Willoughby, R., Cotterell, M., Lin, H., Orr-Ewing, A., & Reid, J. (2017). Measurements of the imaginary component of the refractive index of weakly absorbing single aerosol particles. *Journal of Physical Chemistry A*, *121*(30), 5700-5710. https://doi.org/10.1021/acs.jpca.7b05418

Measurements of the Imaginary Component of the Refractive Index of Weakly Absorbing Single Aerosol Particles

Rose E. Willoughby[1], Michael I. Cotterell[1,2,3], Hongze Lin[4],

Andrew J. Orr-Ewing[1] and Jonathan P. Reid[1]*

[1]School of Chemistry, University of Bristol, Cantock's Close, Bristol BS8 1TS, UK

[2]College for Engineering, Mathematics and Physical Sciences, University of Exeter, EX4 4QF, UK

[3]Aerosol Observation Based Research, Met Office, EX1 3PB, UK

[4] College of Optical Science and Engineering, Zhejiang University, Hangzhou 310058, China

*Author for correspondence: j.p.reid@bristol.ac.uk

Abstract

The interaction of atmospheric aerosols with radiation remains a significant source of uncertainty in modelling radiative forcing. Laboratory measurements of the microphysical properties of atmospherically relevant particles is one approach to reduce this uncertainty. We report a new method to investigate light absorption by a single aerosol particle, inferring changes in the imaginary part of the refractive index with change in environmental conditions (e.g. relative humidity) and inferring the size dependence of the optical extinction cross-section. More specifically, we present measurements of the response of single aerosol particles to near infrared (NIR) laser induced heating at a wavelength 1520 nm. Particles were composed of aqueous NaCl or $(NH_4)_2SO_4$ and were studied over ranges in relative humidity (40 - 85%), particle radius (1 – 2.2 μm) and NIR laser power. The ensuing size change and real component of the refractive index were extracted from measurements of the angular variation in elastically scattered light. From the heating-induced size change at varying NIR beam intensities, we retrieved the change in the imaginary component of the refractive index. In addition, cavity ring-down spectroscopy measurements monitored the change in extinction cross-section with modulation of the heating laser power.

Introduction

The ability of aerosols to scatter and absorb solar and terrestrial radiation is governed by particle size, morphology, mixing state and refractive index (RI). The single scattering albedo (SSA) is an important optical property in determining the net influence of aerosols on the Earth's radiative balance. The SSA is the ratio of the scattering (σ_{sca}) and total extinction (σ_{ext}) cross sections of a particle, with accurate characterizations of these optical quantities of upmost importance for improving the representation of aerosol in climate models.[1] To measure the SSA of aerosol particles, at least two of the three light attenuation coefficients (scattering, absorption and extinction) must be quantified. Providing aerosol particles are homogeneous and spherical, the optical attenuation coefficients and SSA can be calculated using Mie theory for a particle of arbitrary size, if the complex refractive index is known. The complex RI, *m*, consists of a real component (*n*) that influences the extent of light scattering and an imaginary component (*k*) that determines the magnitude of light absorption. For aerosol particles of diameter 150 nm with *n* equivalent to that of ammonium sulfate, Zarzana and co-workers calculated that an uncertainty of ± 0.01 in *k* translates into to an uncertainty of ± 20 % in radiative forcing.[2] Moreover, a reduction in *k* from 0.05 to 0 for secondary organic aerosols (SOA) has been shown to decrease the estimated cooling effect of an aerosol by a factor of 3.[3] These studies emphasize the importance of measuring accurate refractive indices to improve the quantification of the direct contribution by aerosols to radiative forcing.

Aerosol cavity ring-down spectroscopy (A-CRDS) and cavity enhanced extinction spectroscopy (CEES) have been used extensively to measure the extinction coefficients of ensemble aerosol.[4–9] These measurements of aerosol extinction have been used to retrieve the complex refractive index of a range of aerosol species, such as secondary organic aerosol, inorganic species and mineral dust.[6,10–14] Typical uncertainties for A-CRDS for the real component of the RI are $n \pm 0.02$.[9] The size distributions and number concentrations of the ensemble of aerosols are selected prior to extinction measurements, commonly with a differential mobility analyzer, the use of which introduces ~10% uncertainty into the extinction measurements.[15–17] Zarzana *et al.* showed that the RIs retrieved from extinction-only measurements are too inaccurate to merit use in radiative forcing calculations.[2] The same study showed that when more than one attenuation coefficient was

measured, the greater accuracy in the retrieved complex RI significantly improved estimates of radiative forcing.[2]

Many current research methods combine measurements of extinction, scattering and absorption to retrieve superior precision in aerosol refractive index.[15,18,19] Aerosol extinction measurements from CRDS have been combined with scattering measurements from nephelometry to allow the aerosol absorption to be derived from the difference between the two measurements,[20,21] resulting in SSA measurements with an expected associated error of < 2.9%.[15] Photoacoustic spectroscopy (PAS) has been used to measure aerosol absorption,[22] with the upper limit of instrument precision stated as ~ 6%.[18] Combining PAS with CRDS has enabled the complex refractive index of SOA to be studied, with typical uncertainties in $n < \pm 0.006$ and $k < \pm 0.002$.[23] Recent measurements by Bluvshtein and co-authors combined extinction, scattering and absorption measurements from CEES, PAS, CRDS and nephelometry to obtain the SSA of brown carbon proxies from 300-650 nm.[24]

Laboratory studies of single aerosol particles allow the fundamental aerosol microphysical properties to be deduced with enhanced precision. The precise size (to nm accuracy) and microphysical properties of a single particle with a known composition can be measured, thus eliminating additional uncertainty associated with ensemble measurements of aerosol size and number distributions.[9] The optical properties of particles of known composition can be probed with high precision, enabling predictive mixing rules to be compared and assessed.[25] Single aerosol particles have been studied with a number of different experimental techniques. For example, PAS of an optically trapped single aerosol particle was recently proven to be a potentially powerful tool for elucidating photochemical reactions that occur in the atmosphere.[26] Single particle nephelometry has been developed to measure the complex refractive index and distinguish between spherical and non-spherical particles.[27] The absorbing properties of single aerosol particles trapped with aerosol optical tweezers have been retrieved from whispering gallery modes observed by Raman spectroscopy.[28] This technique provided the real refractive index to a precision of ± 0.0012 (better than ± 0.11 %) and, in a limited number of studies, the technique has been shown to be sufficiently sensitive to allow the determination of imaginary refractive indices as small as 1×10^{-8}.[28]

Within the atmosphere, aerosols experience varying environmental conditions, such as changes to relative humidity (RH) which alter the composition of a particle and consequently the physiochemical properties that affect their radiative forcing. It is therefore imperative to study the optical properties of aerosol particles at varying humidities. We have developed a single particle cavity ring-down spectroscopy (SP-CRDS) instrument with demonstrated high precision in the retrieved real component of the refractive index, with a typical uncertainty of ± 0.003 in n.[29] We recently reported a parameterization of the real RI in terms of both RH and wavelength for a variety of inorganic aerosol components.[29] The current work presents a novel strategy to measure simultaneously the extinction and absorption of a single aerosol particle by introducing an additional heating laser beam into our SP-CRDS instrument. This heating laser beam can be used to induce a size change from which the change in k (Δk) can be determined. In many ways the underlying process is similar to the approach used in PAS instruments, except here we report changes to the particle size directly, rather than probe the pressure wave that propagates following heat and mass transfer from an evaporating heated aerosol particle. Here, we present the retrieval of the change in k from single, weakly absorbing aerosol particles at a number of discrete humidities (from ~ 40 - 85% RH). We model the change in particle size, temperature and vapor pressure when a particle is illuminated by wavelengths of 532 and 1500 nm, and laser powers of 20 and 50 mW. We present measurements for aqueous aerosol particles containing the atmospherically relevant inorganic solutes NaCl or $(NH_4)_2SO_4$.

Experimental and Computational Methods

Single particle cavity ring-down spectroscopy instrument

Figure 1 illustrates the SP-CRDS instrument, which has been described previously.[29–33] In this work, an additional NIR laser beam is included to induce droplet heating.

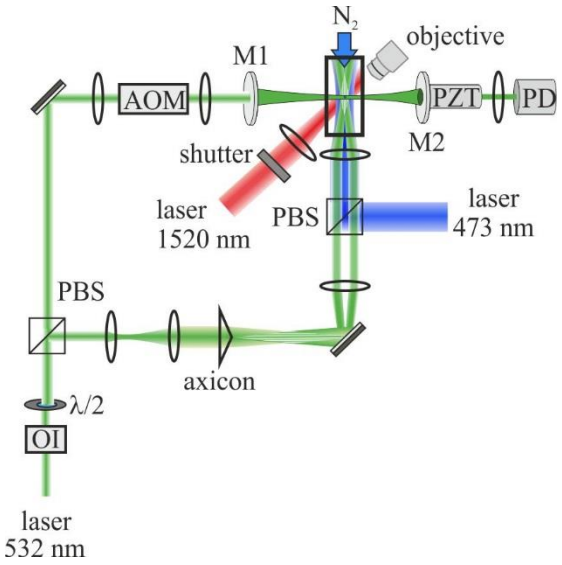

Figure 1: Schematic diagram of the experimental set up. AOM is an acousto-optic modulator, M1 and M2 are highly reflective mirrors constituting the ring-down cavity, PZT is a piezo ring actuator, PD is a photodiode, PBS is a polarizing beam splitter and OI an optical isolator.

A single aerosol particle was optically trapped in a Bessel laser beam (BB, λ = 532 nm) while the surrounding humidity was controlled and held constant. In addition, the particle was continuously illuminated with a second laser beam (λ = 473 nm) with a Gaussian intensity profile, from which the elastically scattered light was collected. Moreover, the particle was irradiated with a near infrared laser beam (λ = 1520 nm) at systematically varied intensities. Finally, CRDS was used to characterize changes in the optical cross-section of the particle (λ = 532 nm).

The Bessel laser beam optical trap

The BB was formed by passing a Gaussian 532 nm laser beam through a 2º axicon, i.e. a conically shaped lens. The resulting beam has a circularly symmetric cross-section consisting of a central core with multiple rings. The BB was focused through two lenses to reduce the BB core to 3-5 µm, in diameter, and was reflected by a 45º mirror to propagate the beam vertically into the trapping cell. A plume of aqueous aerosol was introduced into the trapping cell from a medical nebulizer. A counter-propagating nitrogen gas flow, of controlled humidity and flow rate of ~ 200 sccm, balanced the radiation pressure exerted by the BB to allow a single aerosol particle to be confined for several hours. The radii of single aerosol particles studied in this work ranged from ~ 1 – 2 µm. We ensured that a single particle was trapped in the BB by observing the elastically scattered light

and cavity ring-down (CRD) time. If, occasionally, more than one particle was trapped, the trapping cell was evacuated and aerosol was reintroduced into the trapping cell until only a single particle was trapped.

Retrieval of single particle real refractive index and radius

A Gaussian profile probe laser beam at 473 nm was aligned co-linearly with the BB through a polarizing beam splitter, before being passed through a lens (*f = 50 mm)* which weakly focused the beam into the trapping cell. The probe beam diameter was ~ 8 × the diameter of the BB core. The alignment of the central core of the BB and 473 nm probe beam ensured the probe beam was centered on the trapped particle. A camera coupled to a 20 × microscope objective situated perpendicular to the direction of illumination collected the angular variation in elastically scattered light, referred to the phase function (PF), from the 473 nm illumination. A 532 nm-laser line filter located prior to the camera ensured that only λ = 473 nm light contributed to the phase function images.

PFs were recorded every second and the experimentally measured PFs were fitted to PFs simulated by Mie Theory. This procedure has been described previously.[29,30,34,35] The elastically scattered 473 nm light was recorded as the NIR heating beam irradiated the droplet. The real refractive index at 473 nm and the particle radius were retrieved by comparing the measured PFs with a library of simulated Mie theory PFs. The parameters determining the simulated phase functions were varied according to the equation:

$$n_\lambda = n_{\lambda,0} + \frac{n_{\lambda,1}}{a^3} + \frac{n_{\lambda,2}}{a^6} \qquad 1$$

where n_λ is the refractive index at the wavelength of illumination, $n_{\lambda,0}$ is the refractive index of pure water at wavelength λ, a is the particle radius, and $n_{\lambda,1}$ and $n_{\lambda,2}$ are coefficients that were optimized to achieve a maximum in the mean correlation between measured and simulated PFs. The optimized values of $n_{\lambda,1}$ and $n_{\lambda,2}$ were obtained by a systematic search, followed by a grid search of $n_{\lambda,1}$ and $n_{\lambda,2}$ around the values associated with the highest mean Pearson correlation coefficient from the initial search. Comparison of each measured PF with the simulated PF gave a corresponding correlation value. The entire set of PFs has an associated mean Pearson correlation coefficient, $\bar{c}(n_\lambda)$, where $\bar{c}(n_\lambda) = 1$ would equate to perfect correlation between the sets of measured and simulated PFs. The search parameters were refined to achieve the maximum Pearson

correlation, with this maximum location defining the best fit parameters of particle radii, n_{λ}, $n_{\lambda,1}$ and $n_{\lambda,2}$.

The RH probe was located ~ 10 cm from the droplet, which is significantly further than in measurements we have previously reported. The heating beam, at 1520 nm, is focused into the trapping cell where the RH probe was previously located necessitating a change in RH probe location. Thus, the measurements of RH were not deemed to be reliable, as the probe was located too far from the droplet trapping environment. We previously reported average n_{473} for a number of aqueous inorganic species with ± 2 % uncertainty in RH.[29] Therefore, we instead infer the RH in this study using the measured n_{473} in combination with published RI-RH parameterizations.

Near-IR heating of the single particle.

A near infrared laser beam (1520 nm, NTT Electronics, NLK1S5GAAA) was passed through an optical beam shutter (Thorlabs, SH05) which opened and closed every ~ 20 seconds, thus repeatedly irradiating the particle. The beam was focused by a lens (*f = 40 mm*) and then propagated horizontally into the trapping cell, orthogonal to the PF and BB laser beams, and towards the phase function imaging camera coupled to a high numerical aperture objective.

The alignment procedure for the NIR heating beam was as follows. When a droplet was trapped, the elastically scattered light from the 473 nm beam was observed, using a band pass filter to prevent collection of NIR light. The camera position was optimized to ensure the phase function was at the center of the camera image. The band pass filter was then removed to allow coarse alignment of the NIR beam with the 473 nm elastically scattered light. Finally, the filter was reinstated and the NIR beam alignment was finely adjusted until the change in the positions of the elastic light scattering fringes in the phase function was maximized upon exposure to the NIR beam.

During the measurements with a single particle at constant RH, the heating beam was modulated and the power controlled and varied. The trapped particle was heated for ~ 20 seconds, then the heating beam was shuttered for ~ 20 seconds before the process was repeated at a different laser power. The power of the heating laser was varied such that the particle experienced varying magnitudes of heating, and therefore underwent varying degrees of heating-induced size change.

The heating laser beam waist was retrieved at the particle location from a series of measurements and calculations. The beam waist of the heating beam prior to any focusing lenses was measured by scrolling a razor blade mounted on a micrometer-resolution translation stage across the Gaussian profile of the heating beam to determine the pre-focus beam waist and profile. The laser power associated with each position of the blade was measured with a power meter. The NIR beam was focused through a lens into the trapping cell and the beam waist at the focus calculated to be 3.0 μm from the lens properties and the measured pre-focus beam waist. The distance of the particle from the focal point along the axis of the heating beam was retrieved as follows. A trapped particle was moved along the propagation axis of the heating beam by adjusting the position of the micrometer stage supporting the trapping cell. PFs were measured for the trapped particle at each position along the propagation axis of the heating beam, from which the particle radius was retrieved at each associated position. The change in particle radius corresponded to the position of the particle in the heating beam, with a minimum in radius assumed to occur when the particle experienced the focal point of the heating beam. This combination of methods allowed the heating beam waist to be calculated at a given distance of the droplet from the focal point. This process was repeated a number of times, giving an average beam waist at the particle's location of 81.6 μm, 0.5 mm from focal point (for more information see the supplementary information).

Single particle cavity ring-down spectroscopy

A fourth laser beam was also centered on the aerosol droplet to provide information about any change in extinction cross-section from CRDS measurements. The CRDS was conducted at a wavelength of 532 nm in a spectrometer which has been described previously.[29,31,32,36] The particle was centered in the CRDS beam by optimizing its vertical and horizontal positions. The particle trapping height was then monitored by a camera, and a feedback loop used to control the BB laser power to ensure that the particle remained in the same vertical position within the trapping cell. The phase functions were recorded every second while the particle underwent the modulated heating, whereas the ring down times were measured at a rate of 5-10 Hz.

CRDS was used to explore whether changes in the extinction cross-section were measurable upon laser heating. We previously considered the limitations of the detectable changes in the extinction cross section for a single, absorbing aerosol particle.[37] Here, however, the aerosol particle is non-

absorbing at the CRDS laser wavelength and we instead examine the consequences of absorption at the wavelength of the NIR heating beam for the optical cross-section at the CRDS wavelength.

Modelling the size response of aqueous droplets to laser-induced heating

An aqueous droplet illuminated by a laser beam will be heated through absorption of radiation. Constant laser irradiation raises the droplet temperature until a steady state is reached, such that the energy absorbed by the droplet is equal to energy dissipated through the process of collisional cooling with surrounding gas molecules. At this steady state, there is no net evaporation or condensation of water at the droplet surface, and the droplet size reaches a new equilibrium value. We use the droplet heating model described by Miles *et al*. to predict the size response of aqueous sodium chloride droplets illuminated by an NIR laser beam of wavelength 1500 nm.[28] These authors successfully predicted sodium chloride droplet size responses in optically tweezed aerosol particles for a laser wavelength of 532 nm and used their model to retrieve the complex RI values for single droplets, measuring imaginary refractive indices as small as 10^{-8}. In developing our experimental set-up, we used this model to select the necessary laser wavelength and power to drive observable changes in droplet size in this proof-of-concept study.

For an aqueous droplet of radius a illuminated by a laser of constant power P, the increase in droplet temperature from an initial value T_1 to a temperature T_2 upon laser exposure is described by:[28,38,39]

$$\Delta T = T_2 - T_1 = \frac{aQ_{abs}P}{4\pi w^2 \kappa_a} \qquad 2$$

Here, Q_{abs} is the absorption efficiency, w is the laser beam waist at the position of the droplet and κ_a is the thermal conductivity of air (0.026 W m^{-1} K^{-1} at 298 K). Mie theory is used to predict Q_{abs} for an input value of particle radius, RI and wavelength. The absorption efficiency contains structure from interference and so-called ripple contributions; for illumination wavelengths smaller than the droplet size, sharp resonances in Q_{abs} can cause large increases in the droplet temperature. [28,40,41]

At equilibrium, the vapor pressure of water above a solution droplet surface equals the partial pressure of water in the gas phase. Once heated, the solution droplet will evaporate to regain this thermodynamic criterion for equilibrium: the increase in vapor pressure from heating is counteracted by a vapor pressure reduction due to the increasing concentration of solutes within

the droplet with decreasing size. The Clausius-Clapeyron equation relates the change in vapor pressure of the solution to a change in temperature:

$$ln\left[\frac{p(T_2)}{p(T_1)}\right] = \frac{\Delta H_{vap}}{R}\frac{T_2 - T_1}{T_1 T_2} \quad (3)$$

in which ΔH_{vap} is the enthalpy of vaporisation of the aqueous solution and R is the molar gas constant. Assuming changes in the droplet temperature from laser-induced heating are small, Equation 3 simplifies to:

$$ln\left[\frac{p(T_2)}{p(T_1)}\right] = \frac{\Delta H_{vap}}{R}\frac{\Delta T}{{T_1}^2} \quad (4)$$

with ΔT described by Equation 2. The absolute vapor pressure depends on the activity of water in the solution droplet, a_w, which decreases as water evaporates and the droplet decreases in volume. We incorporate the dependence of vapor pressure on a_w, and define $T_1 = T_a$, the ambient temperature T_a in the absence of laser heating, to obtain the vapor pressure of the heated droplet:

$$p(T_2) = a_w p_{sat}(T_a) exp\left[\frac{\Delta H_{vap}}{R}\frac{\Delta T}{{T_a}^2}\right] \quad (5)$$

Here, $p_{sat}(T_a)$ is the saturation vapour pressure of water above a flat surface at ambient temperature (3235 Pa at 298 K). We used the E-AIM model to describe the dependence of droplet size and solute concentration on a_w.[42,43] We then used calculations from E-AIM to relate the radial growth factor (the ratio of the radius for the solution droplet to that corresponding to the dry salt) to a_w. This allowed simulations of $p(T_2)$ at all values of a_w (and hence radii) over which the solution droplet exists, i.e. from the efflorescence water activity (~0.45 for sodium chloride) to 1.00.

Here, we first verify our model by comparing predictions for λ = 532 nm with previous data reported by Miles *et al*., before considering the influence of NIR illumination (λ = 1500 nm) on particle heating. The model calculations were validated against the simulations of Miles *et al*. using the parameters for their λ = 532 nm optical tweezer experiments.[28] The initial droplet size was set as 3913.3 nm at a corresponding water activity of a_w = 0.9775 to represent typical droplet conditions in the experiments. ΔH_{vap} was set to 44×10^3 J mol^{-1} (i.e. close to the 44.24 kJ mol^{-1} value for a saturated salt solution), T_a was fixed at 300 K and w = 4 μm. The simulations by Miles *et al*. use Mie-Debye spherical aberration theory to predict Q_{abs} for a focused Gaussian beam, while

we used Mie theory to simulation Q_{abs}. We described the real RI of the sodium chloride solution droplet and its dependence on a_w using the parameterization we reported recently,[29] although Miles *et al*. used a parameterization based on electrodynamic balance measurements,[44] and set the imaginary RI to 2.5×10^{-9}. Figure 2(a) shows our calculations of ΔT for λ = 532 nm and a laser power of 20 mW, which gives a temperature elevation of 10s of millikelvin, depending on starting droplet size. Based on these temperature perturbations, Figure 2(b) shows the calculated change in droplet vapor pressure for laser powers of 0, 15, 18 and 20 mW with change in droplet size. The introduction of the laser heating beam induces significant changes to the vapor pressure with resonant enhancement by whispering gallery modes at particular droplet sizes. Our calculations of vapor pressure agree well with those reported by Miles *et al*.

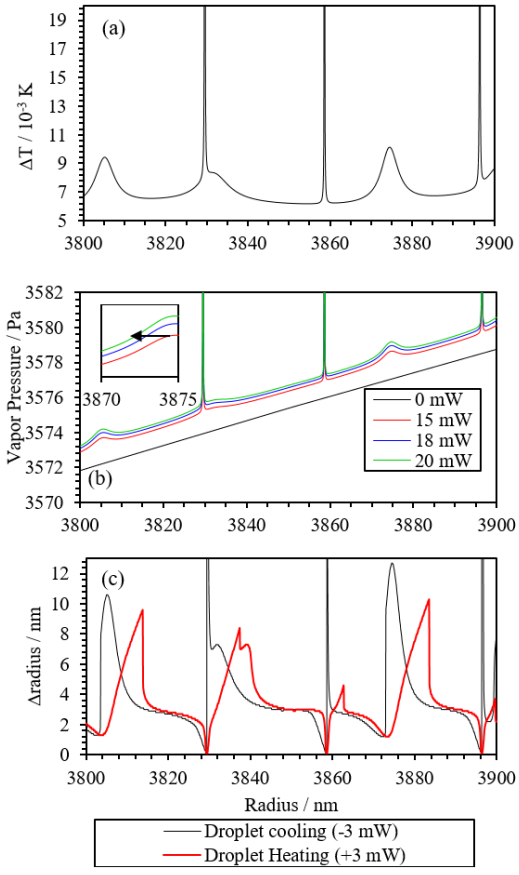

Figure 2: Simulated droplet heating behavior for an aqueous NaCl droplet at an initial a_w = 0.9775, irradiation wavelength λ = 532 nm, and beam waist w = 4 µm. (a) the variation in ΔT with droplet radius for P = 20 mW; (b) calculations of the vapor pressure variation with droplet radius for values of P of 0, 15, 18 and 20 mW; (c) the predicted change in droplet radius (Δradius) for the cases of a decrease in laser power from 18 mW to 15 mW (black line) and an increase in laser power from 15 mW to 18 mW (red line).

We also calculated the change in radius (Δradius) expected when the laser power is modulated between 15 mw and 18 mW. The Δradius values are calculated from an isobaric line on the vapor pressure – radius plot (Figure 2(b)) linking two curves corresponding to different laser powers. The droplet radius axis in Figure 2(c) corresponds to the initial radii of a number of simulated droplets before stepping the laser power and the induced heating. Once equilibrated in size, the droplet has the same vapor pressure before and after the step in laser power, but this vapor pressure is a combination of different degrees of elevation (by heating) and reduction (from solute effects associated with droplet size changes). Figure 2(c) also shows the Δradius for the opposite case of increasing the laser power (heating) by 3 mW, demonstrating the non-reversible changes in Δradius caused by the resonance structure. There are multiple radii at which equal vapor pressure is attained, and the radius change achieved will differ depending on whether the particle is cooling, and the radius is increasing from condensational growth, or the particle is being heated, and the radius is decreasing from evaporative loss.

Having verified that our laser-induced droplet heating model correctly predicts changes in droplet size, we then used it to investigate whether we could resolve changes in droplet size induced by λ = 532 nm laser heating from the Bessel beam optical trap in our SP-CRDS instrument. The change in power density that we can induce in our BB optical trap is comparable to those achievable in the optical tweezer experiments of Miles *et al*. However, we are limited to a maximum RH of ~ 80% in our instrument, caused by the dilution of ambient air by the dry N_2 gas purge flows that pass over the CRDS mirrors. Compared to the RH values of 97.75% used in the experiments of Miles *et al*., our SP-CRDS measurements occur within a regime where the radial growth factor has a very low sensitivity to a_w. Using w = 2 μm, a change in laser power from 30 mW to 35 mW (a typical range achievable for the Bessel beam core power), an initial NaCl particle radius of 2000 nm (the largest typical size we trap in our SP-CRDS instrument) for an initial a_w of 0.8, our heating model predicts Δradius of < 2 nm. This change is too small to resolve with the precision of size retrievals from PFs. Therefore, we now investigate the effectiveness of laser-induced heating using a NIR laser emitting at a wavelength matching a strong absorption band for water in inducing size changes sufficient for detection with PF measurements.

The NIR laser heating experiments reported here drive water evaporation from an aqueous sodium chloride or ammonium sulfate droplet confined in the BB trap of an SP-CRDS instrument. The

heating laser has a much broader focus than in the optical tweezers measurements of Miles *et al*., and the droplet is smaller in size. Instead of investigating the optical absorption in the visible, we measure the imaginary component of the refractive index at 1500 nm. Figure 3(a) shows the variation in the complex RI components with wavelength for water.[45,46] The imaginary RI increases by ~ 3 orders of magnitude from a wavelength of 532 to 1064 nm, and increases by a further 2 orders of magnitude from 1064 to 1500 nm, with a value of $k = 2.57\times10^{-4}$ at λ = 1500 nm. The simulations reported below correspond to a NIR heating beam with λ = 1500 nm.

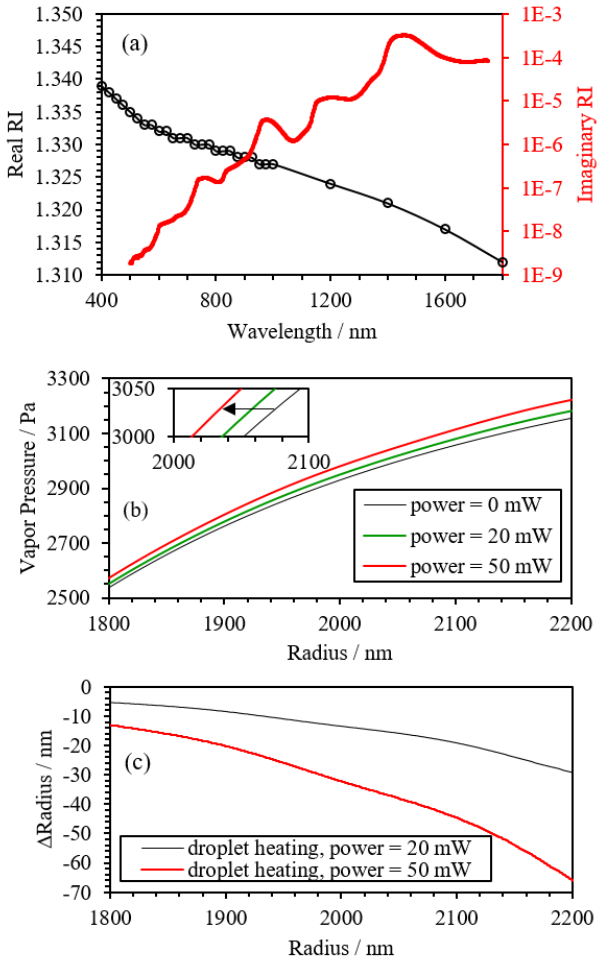

Figure 3: (a) The variation in the real RI[45] and imaginary RI[46] for water over the wavelength range 400 – 1800 nm. Lines are to guide the eye. (b) The calculated vapor pressure for an aqueous NaCl droplet with an initial radius of 1800 nm at an initial a_w of 0.8 upon illumination with a λ = 1500 nm, w = 100 µm laser beam using P values of 0, 20 and 50 mW. (c) The calculated Δradius using the simulations in (b), for a droplet heated from an initial state corresponding to P = 0 mW.

We performed simulations of the droplet vapor pressure and Δradius for λ = 1500 nm and w = 100 µm. For these simulations, we used the aforementioned heating model parameters and methods.

To describe the complex RI of aqueous NaCl droplets at IR wavelengths, we used the RI descriptions for pure water as reported in Figure 3(a). The real RI was set to 1.319 and the imaginary RI set to 2.57×10^{-4}. The reference droplet radius was selected to be 1800 nm at an initial a_w of 0.8 equal to an environmental RH of 80 %, representing typical values for a droplet confined in the SP-CRDS instrument at high RH. We repeated the simulations for the three laser powers of 0, 20 and 50 mW. Figure 3(b) shows the predicted vapor pressure curves over the droplet radius range 1800 – 2200 nm. Unlike the shorter wavelength simulations, there is an absence of resonant structure in the vapor pressures curves because of the long wavelength of the NIR beam compared to the droplet radius, and the much larger value of the imaginary RI, which damps resonant coupling into whispering gallery modes. We calculated Δradius in the heating direction, from a starting droplet with no heating to a droplet illuminated at powers of either 20 or 50 mW. Figure 3(c) shows the expected change in droplet radius upon exposure to the heating beam, with representative values of Δradius of 13.5 nm and 32 nm for P = 20 mW and P = 50 mW, respectively. These size changes are sufficient for detection by PF imaging.

Results and discussion

Near-IR heating of single aerosol particles at high relative humidity

Single aerosol particles composed of both aqueous ammonium sulfate and sodium chloride have been studied. Each particle was trapped, and held at (near) constant RH to retrieve k as a function of RH. The heating laser beam irradiated the particle while the power was modulated and systematically varied in power. Laser illumination of the droplet caused the droplet temperature to increase, thus driving evaporation of water, and an associated heating-induced size change was measured. At each laser power, the 1520 nm laser irradiated the droplet for ~ 20 seconds, which was sufficient time to allow the particle to achieve a steady size, with no further net condensation or evaporation. Figure 4(a) shows the radius response of a single aqueous sodium chloride particle to heating. Upon initiation of heating, the droplet evaporated to its new equilibrium size within 1 second, the limiting detection timescale of PF measurements. A strong correlation can be seen between the incident laser power and the volume of water lost from the droplet, in Figure 4(a) and

(b). The radius of the particle reverted to the original size once the heating beam was attenuated to zero power (black points).

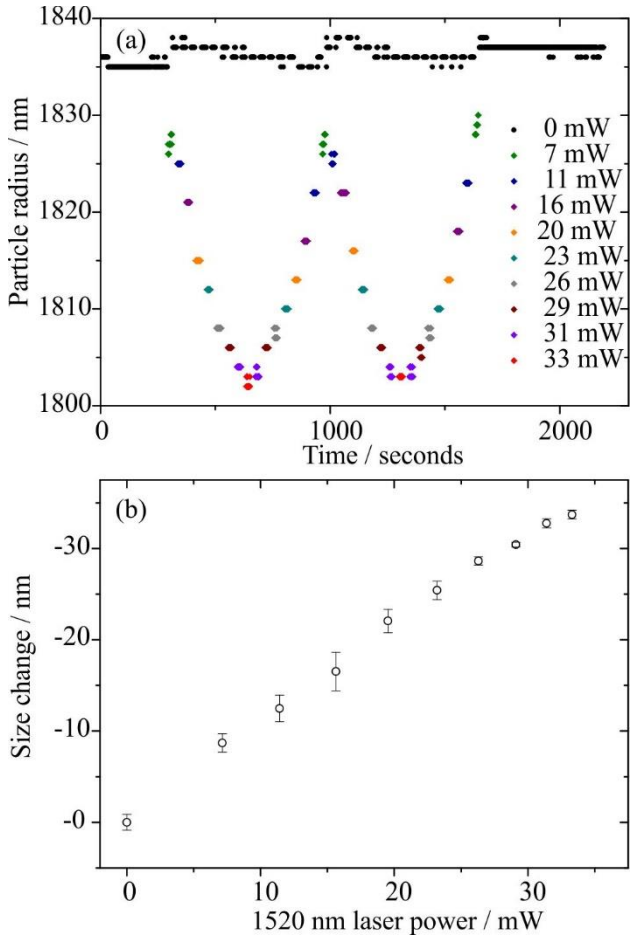

Figure 4: Irradiation of an aqueous NaCl droplet with a 1520-nm laser beam. (a) Changes to the radius of the single aerosol particle as the laser power is varied (indicated by the colored data points). (b) The average change in particle radius as a function of heating laser power. The error bars indicate the standard deviation in the derived radius.

Comparing the simulated NIR heating-induced size change to the measured size change

The heating-induced size changes measured from PFs were compared to the modelled size changes. The simulations required inputs of beam waist (81.6 µm, estimated with the method outlined earlier and described more extensively in the Supplementary Information) and initial water activity (a_w = 0.89, for the particles in Figure 4). The particle radius was 1836 nm without

1520 nm irradiation and the maximum laser power used was 33 mW. However, the calculated size change was approximately double the experimentally measured size change at 33 mW and this was found to be the case for all particles studied. This discrepancy (of ~ 41 nm, for the particle presented in Figure 5) is significantly larger than the uncertainty of ± 0.5 nm associated with PF analysis, suggesting that one of the parameters required for the heating simulation was not correct. The ± 2% uncertainty associated with the retrieved RH only accounts for ± 0.5 nm of size change. The modelled heating-induced size change was more sensitive to the values of beam waist or laser power. Figure 5 shows the sensitivity in the simulated change in radius to these model inputs for the single highest power measurement. In Figure 5(a), the simulated value of the laser power was varied from 5 – 33 mW with the beam waist set at 81.6 µm. In Figure 5(b), the simulated 1520 nm beam waist was varied from 75 – 88 µm while the laser power was held constant at 33 mW. The resultant changes in radius predicted by the model are compared to the measured change in radius of 33 nm recorded at the highest level of NIR power, P = 33 mW (indicated by the blue dashed line).

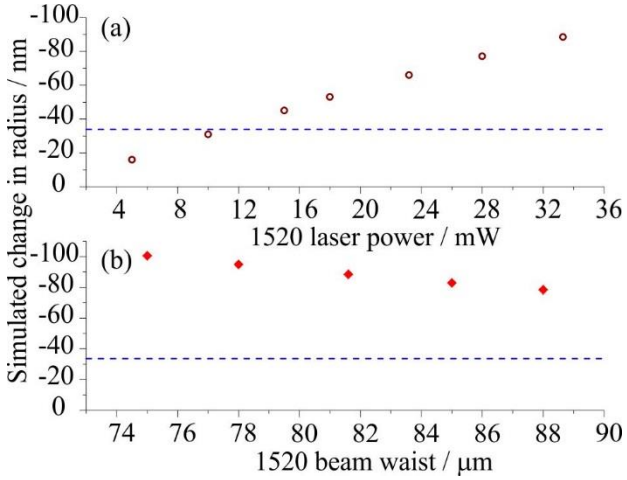

Figure 5: The variation in the modelled heating-induced size change (with inputs of initial size = 1836 nm, a_w = 0.89, initial laser power = 0 mW) as the following input parameters were varied: (a) final laser power (mW), with the beam waist set to 81.6 µm and (b) beam waist (75 – 88 µm), with the final laser power set at 33 mW. The experimentally measured size change of a droplet of 1836 nm at a_w = 0.89 and laser power 33 mW is indicated by the dashed blue line.

From Figure 5, the simulated heating-induced size change is significantly more sensitive to changes in the input laser power than the input heating beam waist. The range of values of beam waist chosen corresponds to the uncertainty associated with the measurements of the NIR beam waist. Therefore, we deduce that the particle must be sampling less than the expected fraction of the full laser power (33 mW) calculated by comparing the beam waist and the particle radius.

Instead, we must base our analysis on inferring changes in absorption and k with RH and size relative to measurements for a droplet at one reference RH, chosen here to be the highest RH. At this reference RH, we assume that the value of k is equal to that of pure water at the highest RH and calculates the effective laser power that gives the observed size change at this RH. This retrieved value of effective laser power is then input for measurements at lower RHs while k_{1520} is varied in the model simulations.

For the data presented in Figure 4, the derived effective total laser power incident on the trapped aqueous NaCl droplet corresponds to 11.0 mW, which is a third of the value expected based on the measured total power output from the 1520 nm beam. This scaling of the actual to effective laser power was retained in further model simulations for all subsequent particle measurements at lower humidities. The scaling accounts for the imperfect transverse and axial positioning of the droplet in the focused Gaussian beam; although a more exact model could be implemented, the current challenge is one of experimental alignment. A particle of ~1 μm size held within a vertically propagating Bessel beam core of similar size and co-propagating beam for PF determination, must be aligned simultaneous with a horizontally propagating CRD beam of waist ~200 μm, the orthogonally propagating NIR laser beam with a focal waist estimated an <10 μm. For particles at lower humidities (i.e. all particles other than the initial reference particle from which the effective laser power was calculated), the value of k_{1520} input into the model was varied, thus allowing a relative change in k_{1520} from that of pure water to be calculated. This approach does enable the relationships between k_{1520}, droplet size and RH to be examined.

Figure 6 shows the outcome of experimentally varying the laser power on the value of n_{473} retrieved from the PF measurements at 473 nm, and the modelled temperature and vapor pressure for two aqueous NaCl droplets held at 89 % and 70% RH. As the NIR laser power illuminating the particle increases, n_{473} also increases, as expected for a decreasing droplet size and increasing solute concentration. Similarly, the retrieved n_{473} of the particle at 70% RH is higher than that of the particle at 89% RH, again due to the higher concentration of solute at lower RH. The concomitant changes in vapor pressure and temperature for each particle were retrieved from model simulations (at the appropriate conditions of e.g. RH). The simulated change in particle temperature is always < 0.1 K, but is larger for higher NIR laser powers, as expected.

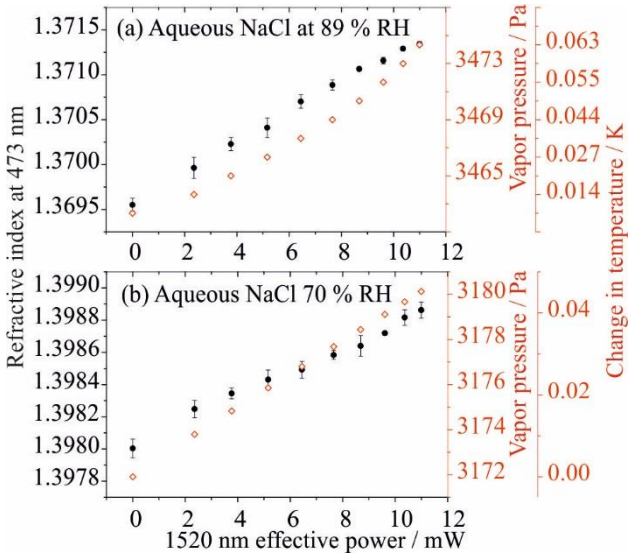

Figure 6: The effect of 1520 nm laser power (scaled to an effective power, as described in the main text) on the average (from up to 7 measurements at each laser power) real refractive index retrieved from fitting PFs at λ = 473 nm to Mie theory predictions (black data points), and the simulated vapor pressure (red data points) and corresponding temperature change (additional axis) for 2 different aqueous NaCl particles held at different humidities.

We report average values of n_{473} in Figure 6, retrieved from multiple measurements of n_{473} at each effective laser power as the power was systematically increased and decreased and repeatedly modulated; a standard deviation of $< \pm 0.00006$ is indicated by the error bars. At any one laser power, there is variation in n_{473} because the particle was exposed to each laser power multiple times (shown in Figure 4) over ~2000 seconds. Over the course of the measurement, drift in RH alters the particle composition and thus the retrieved n_{473}. Considering the timescale of the experiment and slight variations in RH, the modest standard deviations in retrieved n_{473} values illustrate the precision of our technique. The changes in temperature and vapor pressure (red data points in Figure 6) are inferred from the model simulations.

Retrieving the imaginary component of the refractive index of aqueous NaCl and $(NH_4)_2SO_4$ aerosol particles with varying humidity

Single particles composed of aqueous NaCl were held at a discrete RH while the laser power irradiating the particle was varied. The heating-induced size-change was normalized by converting it to a change in growth factor which allowed the variation in size change as a function of RH to

be examined over many droplets of different absolute size. The radial growth factor is defined as the ratio of the wet droplet radius to the dry particle radius and the change is growth factor (ΔGF) is given by:

$$\Delta GF = \frac{a_0 - a_x}{a_{dry}} \quad (6)$$

where a_0 is the radius of a given particle when not illuminated by the NIR beam, a_x is the radius of the same particle at a given NIR laser power of $P = x$ mW, and a_{dry} is the dry size calculated for each particle. The variation in the radial growth factor with RH was calculated from the E-AIM model.[42,43] Then, from comparing the calculated growth factor dependence on RH with the experimental variation in wet droplet size with RH in the absence of the NIR beam, the dry particle size was determined. Finally, the change in growth factor on illumination was calculated from Equation (6).

Figure 7(a) shows the change in GF for 7 different droplets held at RHs in the range 59 – 89 % while the power of the NIR beam was varied. The magnitude of change in GF can be seen to depend systematically on RH. The RH is indicative of the composition of the particle: at lower RHs, the particle solute concentration is higher (a_w is lower), and greater laser power is required to drive the same amount of water evaporation, compared to an equivalent sized particle at higher RH. Therefore, the relative magnitude of change in GF is smaller as the surrounding RH decreases.

The variation in the imaginary component of the refractive index with RH was retrieved by simulating size changes for a range of Δk_{1520} values, and comparing the changes in simulated and measured size changes with laser power at each RH. The retrieved value of k_{1520} represents the change in k_{1520} (Δk_{1520}) from that at the reference RH rather than an absolute value, shown in Equation 7:

$$\Delta k_{1520} = k_{1520}(measurement\ at\ RH) - k_{1520}(reference) \quad (7)$$

where k_{1520} *(reference)* is the imaginary component of pure water that is input in the reference measurement at the highest humidity, from which the effective laser power is determined. In this analysis, the other input parameters were kept constant while Δk_{1520} was varied. The results are shown in Figure 7(b). Although this method does not give the absolute value of k_{1520} it does enable the dependence of $\Delta\ k_{1520}$ on RH to be examined.

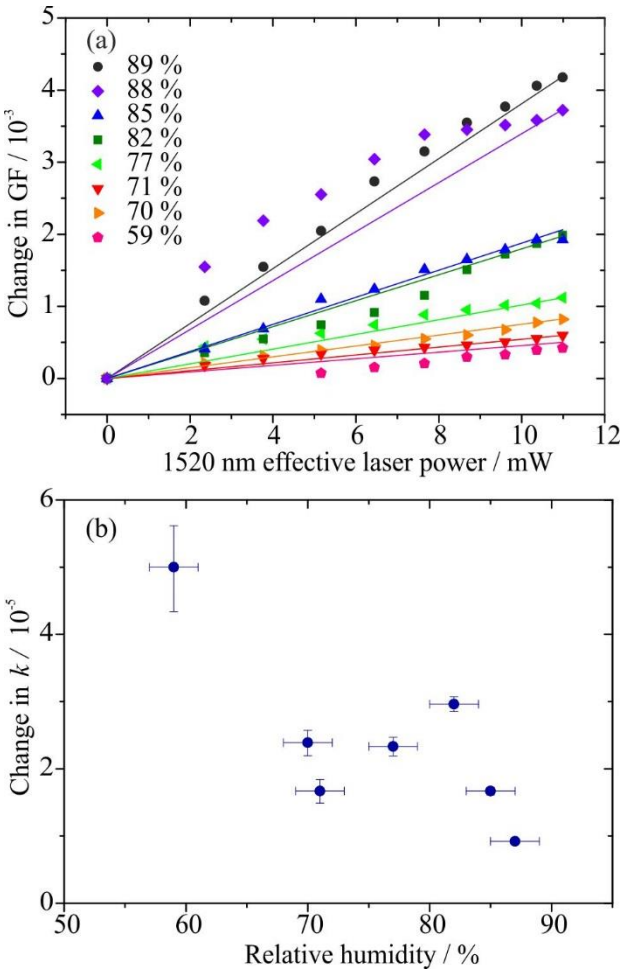

Figure 7: (a) Variation in the change of growth factor for aqueous NaCl particles as a function of the effective heating laser beam power for RHs from 59-89%. The lines correspond to the model prediction of the particle heating-induced size change converted to the GF domain; (b) the retrieved change in k_{1520} for aqueous NaCl particles as a function of RH. The x-axis error bars correspond to the ± 2% uncertainty in RH, and the y-axis error bars represent the uncertainty associated with the retrieved size from PF fitting.

The data plotted in Figure 7(b) suggest a change in k_{1520} for aqueous NaCl droplets as the humidity decreases. This trend is indicative of the particle composition, which is in equilibrium with the surrounding gas phase: as the humidity decreases, the water content of the particle also decreases, which increases the solute concentration. We assume that the light absorption responsible for the observed Δk_{1520} is caused by impurities in the NaCl solute, because NaCl does not absorb at 1520 nm, and this absorption is additional to that of pure water (which is already accounted for in the initial simulations of the reference particle).[47] Miles *et al*. also studied the light absorption of single aqueous NaCl particles at 532 nm with Raman spectroscopy.[28] Their retrieved values of k_{532} were

larger than that of pure water, and this difference was also attributed to the presence of absorbing impurities.[28]

The error bars in Figure 7(b) represent the uncertainty associated with the inferred RH and the retrieved particle size. Fitting the measured PFs with Mie theory yielded the radius and n_{473} values for each particle. Measurements were only included in this work when $\bar{c}(n_{473}) > 0.99$. The uncertainty in the size of the particle retrieved from PF measurements was ± 0.5 nm. The impact of this uncertainty in the retrieved value of Δk_{1520} was assessed by fitting Δk_{1520} to the experimentally measured size change ± 0.5 nm. The resulting uncertainties in the retrieved values of Δk_{1520} are shown in Figure 7(b). The smaller the initial size of the droplet, the larger is the uncertainty in Δk_{1520}.

Figure 8 shows the variation in the Δk_{1520} for a single aqueous $(NH_4)_2SO_4$ particle over a range of RHs, with the highest RH measurement again serving to provide the reference point for the scaling needed to deduce the effective NIR laser beam power. Unlike the case of aqueous sodium chloride aerosol shown in Figure 7, these measurements were made on the same particle and clearly show that Δk_{1520} increases as RH decreases. The magnitude of the change in k_{1520} with RH is comparable to that of aqueous NaCl. The variation of k_λ with wavelength for $(NH_4)_2SO_4$ crystals was reported previously, and the nearest value to our measurement wavelength is at $\lambda = 1500$ nm where $k_{1500} = 3.4 \times 10^{-5}$.[48] This is of the same order of magnitude as our reported change in k_{1520} from that of water with decreasing RH. Measurements of the absolute imaginary component of the refractive index are of greater interest than a relative measure of Δk_{1520}. However, here the importance of measuring the variation in Δk_{1520} with RH, even for very weakly absorbing species, is highlighted. Further work will endeavor to measure k_λ directly as a function of RH, for a wider range of droplet compositions, to parameterize the dependence of k_λ on RH.

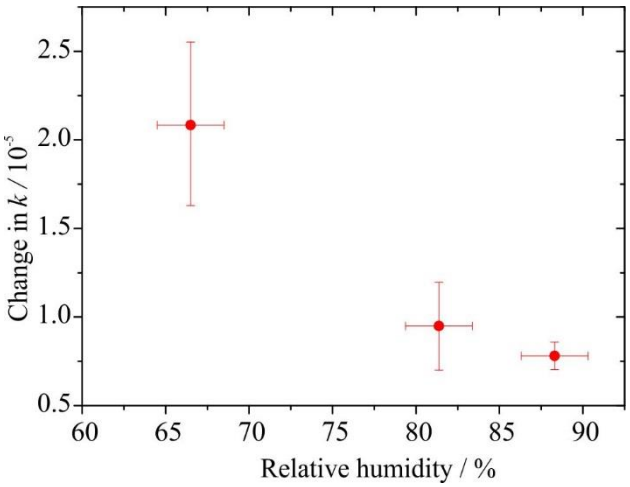

Figure 8: The change in the relative value of k_{1520} for a single aqueous $(NH_4)_2SO_4$ particle held at a range of humidities.

Measurements of the extinction cross-section of a heated single particle

Single particle cavity ring-down spectroscopy measurements were performed for each particle as it was irradiated with the heating beam, and a section of a measurement is shown in Figure 9(a) as an example. The cavity ring-down times, τ, are used to determine the extinction cross-section of the single particle, where:

$$\sigma_{ext} = \frac{L\pi w^2}{c}\left(\frac{1}{\tau} - \frac{1}{\tau_0}\right) \qquad 8$$

where L is the length of the optical cavity, w is the beam waist (of the CRD beam, and estimated as 0.24 mm in later estimates of σ_{ext}), and τ_0 the cavity ring down time of the optical cavity in the absence of the droplet.[49] CRDS measurements were made at a wavelength of 532 nm, where the particle is non-absorbing. Figure 9(a) shows variation in τ as the particle was heated by the NIR laser beam, and illustrates the sensitivity to changes in the particle extinction cross-section induced by the heating. The changes in the recorded cavity ring-down times increase as the power of the heating beam increases. The fluctuations in τ are a consequence of Brownian motion of the aerosol particle within the BB trap.[32,50]

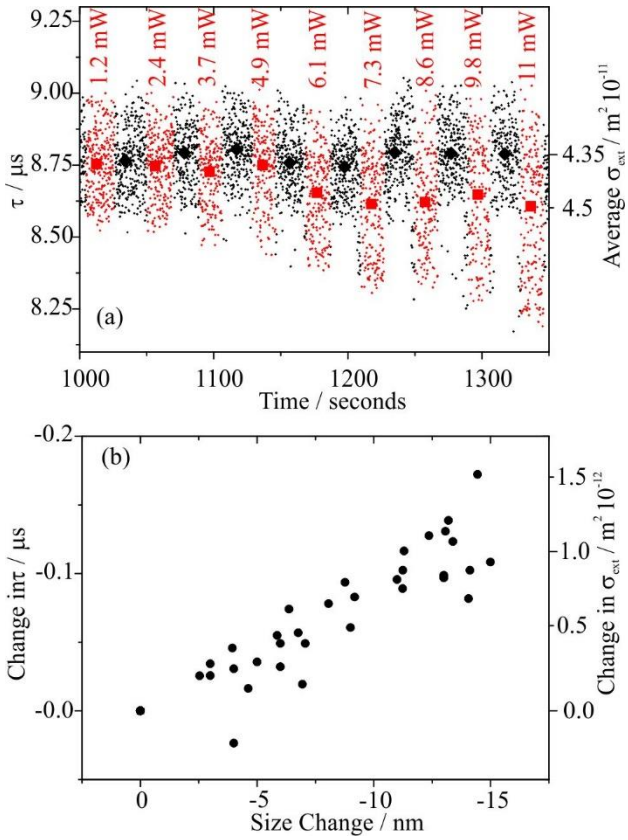

Figure 9: (a) The cavity ring-down times, τ, of a single aqueous NaCl particle as it was heated by a 1520 nm beam (red points) decrease compared to when the 1520 nm beam was blocked (black points). The 1520 nm effective laser power is indicated with red labels. The average τ values at each effective laser power are shown by large red squares, and when the NIR beam is off by the large black diamonds. The average (large red and black) points also correspond to the average estimated σ_{ext} indicated on the corresponding y-axis. (b) The measured τ values and the associated estimated change in σ_{ext} are shown as a function of the particle size change, retrieved from PF measurements, as a result of modulated heating.

Figure 9(a) shows the average measured ring-down time τ, which decreases as the particle is irradiated with increasing NIR illumination. As the particle size decreases, its smaller geometric cross section might be expected to cause an increase in the τ value. However, the τ value is determined by the extinction cross section, not the geometric cross section. These two parameters are connected by the extinction efficiency, Q_{ext}, in which is defined in Equation 9. Q_{ext} is a function of the size parameter, χ (shown in Equation 10).

$$Q_{ext} = \frac{\sigma_{ext}}{\sigma_{geom}} \qquad 9$$

$$\chi = \frac{\pi D}{\lambda} \qquad 10$$

Here, D is the particle diameter and λ is the wavelength of illumination. The extinction efficiency varies with size parameter; thus, as the particle is heated and the size parameter changes, the particle will exhibit different extinction efficiencies. In the size parameter range of the particle considered in the current example, as the particle is heated the extinction efficiency increases with decrease in size. The resulting increase in σ_{ext} causes the observed changes to τ values upon heating.

The rapid heating-induced size response was generally recorded more rapidly by CRDS than by the PF measurements, and observed before the change in the electronic signal reporting the status of the shutter controlling the heating beam was registered. Both the PF and shutter status data were collected every second. This effect is particularly evident in Figure 9(a) at times around 1210 seconds, where the τ values have changed, but the data points are still color-coded as black. Thus, the CRDS data illustrate the rapid size response of the droplets to irradiation by the heating beam, and indicate the benefits that would derive from measuring PFs and the shutter status at intervals of < 1 second.

Figure 9(b) shows the consequences of changes in the power of the heating beam for measured τ values, and change in σ_{ext} values from CRDS and droplet sizes measured from PFs. There is a clear correlation between the changes in τ, σ_{ext} and particle size change induced by droplet heating, each of which is retrieved from separate measurement techniques (CRDS and PFs respectively). This trend reinforces the sensitivity of both phase function measurements and cavity ring-down spectroscopy to changes in the size of single aerosol particles, and further illustrates the complementary use of these techniques. Here we have demonstrated the possibility of providing concurrent extinction cross-section measurements by CRDS when exploring optically induced heating. A fuller analysis of this approach will be the focus of a subsequent paper.

Conclusions:

Droplet heating by a NIR laser has been combined with our previously reported single-particle trapping and observation methods to measure RH-dependent changes in complex refractive index of weakly absorbing single aerosol particles. The absorption of 1520-nm laser radiation by single particles composed of aqueous NaCl or $(NH_4)_2SO_4$ has been reported at a range of discrete RHs.

The size and real component of the refractive index of the particle were retrieved from phase function measurements, and the absorption of a particle relative to a water droplet was calculated from the change in particle size upon heating. The positioning of the single particle in the heating beam proved to be crucial in quantitatively accounting for the size change upon heating and this challenge must be addressed in future work, despite the critical tolerances in aligning multiple laser beams with a trapped droplet that must be achieved. However, here we have developed a method to scale the incident laser power to quantify the actual power irradiating the particle and to retrieve relative changes in absorption. Multiple measurements of single particles of aqueous NaCl, and a single aqueous $(NH_4)_2SO_4$ particle showed an increase in k_{1520} relative to that of water with decreasing RH. This greater absorption at 1520 nm at lower RHs was attributed to impurities in the solute. The measurements illustrate the capability of the system to retrieve Δk_{1520} values for very weakly absorbing aerosol. Despite determining a relative change in k_{1520} rather than an absolute value, the data highlight the variation in the absorption of aerosol particles with RH, thus emphasizing this dependence as an additional factor to be considered when including aerosol optical properties in radiative transfer models.

The detection of changes to the extinction cross-section of a single particle of radius 1-2 μm as the heating beam was modulated demonstrates the sensitivity of our SP-CRDS technique. The changes in geometric cross-section derived from phase function measurements, and changes in extinction cross-section from cavity ring-down spectroscopy, illustrate the complementary nature of these analysis methods. In addition, the CRDS measurements can be made with extremely high time resolution. Such measurements could be invaluable in measuring kinetic parameters for water condensation/evaporation, for example in retrieving the value of the mass accommodation coefficient from measurements on single particles that are much smaller than previously studied.[51,52] In addition, these measurements will allow us to look at the mechanism inherent to photoacoustic spectroscopy, potentially allowing us to study the ambiguities that arise in PAS measurements at elevated RH when the photoacoustic signal is a product of mass transfer from an evaporating droplet as well as heat transport.[53] Further applications will include retrieval of complex refractive index information for more strongly absorbing aerosol species for inclusion in radiative transfer models.

Supporting Information

The Supporting Information provides further description of the heating laser beam waist retrieval, and further discussion on the retrieval of the effective laser power.

Acknowledgments

REW acknowledges funding from GW4+ DTP from NERC (NE/L002434/1) and support from the Aerosol Society in the form of the CN Davies Award. MIC acknowledges funding from NERC and the RSC through an Analytical Trust Fund studentship (NE/J01754X/1) and support from the Aerosol Society in the form of a CN Davies award.

References

(1) Boucher, O.; Randall, D.; Artaxo, P.; Bretherton, C.; Feingold, G.; Forster, P.; Kerminen, V.-M. V.-M.; Kondo, Y.; Liao, H.; Lohmann, U.; et al. Clouds and Aerosols. *Clim. Chang. 2013 Phys. Sci. Basis. Contrib. Work. Gr. I to Fifth Assess. Rep. Intergov. Panel Clim. Chang.* **2013**, 571–657.

(2) Zarzana, K. J.; Cappa, C. D.; Tolbert, M. A. Sensitivity of Aerosol Refractive Index Retrievals Using Optical Spectroscopy. *Aerosol Sci. Technol.* **2014**, *48* (11), 1133–1144.

(3) Moise, T.; Flores, J. M.; Rudich, Y. Optical Properties of Secondary Organic Aerosols and Their Changes by Chemical Processes. *Chem. Rev.* **2015**, *115* (10), 4400–4439.

(4) Wang, L.; Wang, W. G.; Ge, M. F. Extinction Efficiencies of Mixed Aerosols Measured by Aerosol Cavity Ring down Spectrometry. *Chinese Sci. Bull.* **2012**, *57* (20), 2567–2573.

(5) Beaver, M.; Garland, R. A Laboratory Investigation of the Relative Humidity Dependence of Light Extinction by Organic Compounds from Lignin Combustion. *Environ. Res. Lett.* **2008**, *3* (4), 045003.1-045003.8.

(6) Veghte, D. P.; Altaf, M. B.; Haines, J. D.; Freedman, M. A. Optical Properties of Non-Absorbing Mineral Dust Components and Mixtures. *Aerosol Sci. Technol.* **2016**, *6826*, 1–14.

(7) Baynard, T.; Garland, R. M.; Ravishankara, A. R.; Tolbert, M. A.; Lovejoy, E. R. Key Factors Influencing the Relative Humidity Dependence of Aerosol Light Scattering.

623 *Geophys. Res. Lett.* **2006**, *33* (6), 3–6.

624 (8) Li, K.; Wang, W.; Ge, M.; Li, J.; Wang, D. Optical Properties of Secondary Organic
625 Aerosols Generated by Photooxidation of Aromatic Hydrocarbons. *Sci Rep* **2014**, *4*,
626 4922.1-4922.9.

627 (9) Mason, B. J.; King, S.-J.; Miles, R. E. H.; Manfred, K. M.; Rickards, A. M. J.; Kim, J.;
628 Reid, J. P.; Orr-Ewing, A. J. Comparison of the Accuracy of Aerosol Refractive Index
629 Measurements from Single Particle and Ensemble Techniques. *J. Phys. Chem. A* **2012**,
630 *116* (33), 8547–8556.

631 (10) Riziq, A. A.; Erlick, C.; Dinar, E.; Rudich, Y. Optical Properties of Absorbing and Non-
632 Absorbing Aerosols Retrieved by Cavity Ring down (CRD) Spectroscopy. *Atmos. Chem.*
633 *Phys. Discuss.* **2006**, *6* (6), 12347–12387.

634 (11) Dinar, E.; Abo Riziq, A.; Spindler, C.; Erlick, C.; Kiss, G.; Rudich, Y. The Complex
635 Refractive Index of Atmospheric and Model Humic-Like Substances (HULIS) Retrieved
636 by a Cavity Ring Down Aerosol Spectrometer (CRD-AS). *Faraday Discuss.* **2008**, *137*,
637 279–295.

638 (12) Michel Flores, J.; Bar-Or, R. Z.; Bluvshtein, N.; Abo-Riziq, A.; Kostinski, A.; Borrmann,
639 S.; Koren, I.; Koren, I.; Rudich, Y. Absorbing Aerosols at High Relative Humidity:
640 Linking Hygroscopic Growth to Optical Properties. *Atmos. Chem. Phys.* **2012**, *12* (12),
641 5511–5521.

642 (13) Lang-Yona, N.; Rudich, Y.; Segre, E.; Dinar, E.; Abo-Riziq, A. Complex Refractive
643 Indices of Aerosols Retrieved by Continuous Wave-Cavity Ring Down Aerosol
644 Spectrometer. *Anal. Chem.* **2009**, *81*, 1762–1769.

645 (14) Flores, J. M.; Washenfelder, R. A.; Adler, G.; Lee, H. J.; Segev, L.; Laskin, J.; Laskin, A.;
646 Nizkorodov, S. A.; Brown, S. S.; Rudich, Y. Complex Refractive Indices in the near-
647 Ultraviolet Spectral Region of Biogenic Secondary Organic Aerosol Aged with Ammonia.
648 *Phys. Chem. Chem. Phys.* **2014**, *16* (22), 10629–10642.

649 (15) Singh, S.; Fiddler, M. N.; Smith, D.; Bililign, S. Error Analysis and Uncertainty in the
650 Determination of Aerosol Optical Properties Using Cavity Ring-down Spectroscopy,

Integrating Nephelometry, and the Extinction-Minus-Scattering Method. *Aerosol Sci. Technol.* **2014**, *48* (12), 1345–1359.

(16) Toole, J. R.; Renbaum-Wolff, L.; Smith, G. D. A Calibration Technique for Improving Refractive Index Retrieval from Aerosol Cavity Ring-Down Spectroscopy A Calibration Technique for Improving Refractive Index Retrieval from Aerosol Cavity Ring-Down Spectroscopy. **2013**, *6826*.

(17) Miles, R. E. H.; Rudic, S.; Orr-Ewing, A. J.; Reid, J. P. Influence of Uncertainties in the Diameter and Refractive Index of Calibration Polystyrene Beads on the Retrieval of Aerosol Optical Properties Using Cavity Ring Down Spectroscopy. **2010**, *114*, 7077–7084.

(18) Lack, D. A.; Lovejoy, E. R.; Baynard, T.; Pettersson, A.; Ravishankara, A. R. Aerosol Absorption Measurement Using Photoacoustic Spectroscopy: Sensitivity, Calibration, and Uncertainty Developments. *Aerosol Sci. Technol.* **2006**, *40* (9), 697–708.

(19) Zhao, W.; Xu, X.; Dong, M.; Chen, W.; Gu, X.; Hu, C.; Huang, Y.; Gao, X.; Huang, W.; Zhang, W. Development of a Cavity-Enhanced Aerosol Albedometer. *Atmos. Meas. Tech.* **2014**, *7* (8), 2551–2566.

(20) Onasch, T. B.; Massoli, P.; Kebabian, P. L.; Hills, F. B.; Bacon, F. W.; Freedman, A. Single Scattering Albedo Monitor for Airborne Particulates. *Aerosol Sci. Technol.* **2015**, *49* (September), 267–279.

(21) Li, L.; Chen, J.; Chen, H.; Yang, X.; Tang, Y.; Zhang, R. Monitoring Optical Properties of Aerosols with Cavity Ringdown Spectroscopy. *J. Aerosol Sci.* **2011**, *42* (4), 277–288.

(22) Utry, N.; Ajtai, T.; Pinter, M.; Tombacz, E.; Illes, E.; Bozoki, Z.; Szabo, G. Mass-Specific Optical Absorption Coefficients and Imaginary Part of the Complex Refractive Indices of Mineral Dust Components Measured by a Multi-Wavelength Photoacoustic Spectrometer. *Atmos. Meas. Tech.* **2015**, *8* (1), 401–410.

(23) Nakayama, T.; Sato, K.; Matsumi, Y.; Imamura, T.; Yamazaki, A.; Uchiyama, A. Wavelength and NOx Dependent Complex Refractive Index of SOAs Generated from the Photooxidation of Toluene. *Atmos. Chem. Phys.* **2013**, *13* (2), 531–545.

(24) Bluvshtein, N.; Michel Flores, J.; Segev, L.; Rudich, Y. A New Approach for Retrieving the UV-Vis Optical Properties of Ambient Aerosols. *Atmos. Meas. Tech.* **2016**, *9* (8), 3477–3490.

(25) Cai, C.; Miles, R. E. H.; Cotterell, M. I.; Marsh, A.; Rovelli, G.; Rickards, A. M. J.; Zhang, Y. H.; Reid, J. P. Comparison of Methods for Predicting the Compositional Dependence of the Density and Refractive Index of Organic-Aqueous Aerosols. *J. Phys. Chem. A* **2016**, *120* (33), 6604–6617.

(26) Cremer, J. W.; Thaler, K. M.; Haisch, C.; Signorell, R. Photoacoustics of Single Laser-Trapped Nanodroplets for the Direct Observation of Nanofocusing in Aerosol Photokinetics. *Nat. Commun.* **2016**, *7*, 10941.1-10941.7.

(27) Nakagawa, M.; Nakayama, T.; Sasago, H.; Ueda, S.; Venables, D. S.; Matsumi, Y. Design and Characterization of a Novel Single-Particle Polar Nephelometer. *Aerosol Sci. Technol.* **2016**, *50* (4), 392–404.

(28) Miles, R. E. H.; Walker, J. S.; Burnham, D. R.; Reid, J. P. Retrieval of the Complex Refractive Index of Aerosol Droplets from Optical Tweezers Measurements. *Phys. Chem. Chem. Phys.* **2012**, *14* (9), 3037–3047.

(29) Cotterell, M. I.; Willoughby, R. E.; Bzdek, B. R.; Orr-Ewing, A. J.; Reid, J. P. A Complete Parameterization of the Relative Humidity and Wavelength Dependence of the Refractive Index of Hygroscopic Inorganic Aerosol Particles. *Atmos. Chem. Phys. Discuss.* **2017**, No. April, 1–27.

(30) Cotterell, M. I.; Preston, T. C.; Mason, B. J.; Orr-Ewing, A. J.; Reid, J. P. Extinction Cross Section Measurements for a Single Optically Trapped Particle. *Proc. SPIE* **2015**, *9548*.

(31) Mason, B. J.; Walker, J. S.; Reid, J. P.; Orr-Ewing, A. J. Deviations from Plane-Wave Mie Scattering and Precise Retrieval of Refractive Index for a Single Spherical Particle in an Optical Cavity. *J. Phys. Chem. A* **2014**, 2083–2088.

(32) Walker, J. S.; Carruthers, A. E.; Orr-Ewing, A. J.; Reid, J. P. Measurements of Light Extinction by Single Aerosol Particles. *J. Phys. Chem. Lett.* **2013**, *4*, 1748–1752.

(33) Preston, T. C.; Mason, B. J.; Reid, J. P.; Luckhaus, D.; Signorell, R. Size-Dependent Position of a Single Aerosol Droplet in a Bessel Beam Trap. *J. Opt.* **2014**, *16* (2), 25702.

(34) Cotterell, M. I.; Mason, B. J.; Preston, T. C.; Orr-Ewing, A. J.; Reid, J. P. Optical Extinction Efficiency Measurements on Fine and Accumulation Mode Aerosol Using Single Particle Cavity Ring-Down Spectroscopy. *Phys. Chem. Chem. Phys.* **2015**, *17* (24), 15843–15856.

(35) Preston, T. C.; Reid, J. P. Angular Scattering of Light by a Homogeneous Spherical Particle in a Zeroth-Order Bessel Beam and Its Relationship to Plane Wave Scattering. *J. Opt. Soc. Am. A* **2015**, *32* (6), 1053–1062.

(36) Mason, B. J.; Cotterell, M. I.; Preston, T. C.; Orr-Ewing, A. J.; Reid, J. P. Direct Measurements of the Optical Cross Sections and Refractive Indices of Individual Volatile and Hygroscopic Aerosol Particles. *J. Phys. Chem. A* **2015**, *119* (22), 5701–5713.

(37) Cotterell, M. I.; Preston, T. C.; Orr-Ewing, A. J.; Reid, J. P. Assessing the Accuracy of Complex Refractive Index Retrievals from Single Aerosol Particle Cavity Ring-Down Spectroscopy. *Aerosol Sci. Technol.* **2016**, *50* (10), 1077–1095.

(38) Chan, C. H. Effective Absorption for Thermal Blooming due to Aerosols. *Appl. Phys. Lett.* **1975**, *26* (11), 628–630.

(39) Lin, H.-B.; Campillo, A. J. Photothermal Aerosol Absorption Spectroscopy. *Appl. Opt.* **1985**, *24* (3), 422–433.

(40) Miles, R. E. H.; Guillon, M.; Mitchem, L.; McGloin, D.; Reid, J. P. The Influence of Resonant Absorption and Heating on the Equilibrium Size of Aqueous-Solute Aerosol Droplets. *Phys. Chem. Chem. Phys.* **2009**, *11* (33), 7312–7317.

(41) Guillon, M.; Miles, R. E. H.; Reid, J. P.; McGloin, D. Thermo-Optical Resonance Locking of an Optically Trapped Salt-Water Microdroplet. *New J. Phys.* **2009**, *11* (103041), 1–10.

(42) Clegg, S. L.; Wexler, A. S. http://www.aim.env.uea.ac.uk/aim/model3/mod3rhw.php http://www.aim.env.uea.ac.uk/aim/model3/mod3rhw.php (accessed Jan 1, 2016).

(43) Clegg, S. L.; Brimblecombe, P.; Wexler, A. S. A Thermodynamic Model of the System

734 H+ -NH4+ -Na+ -SO42- -NO3− -Cl− -H2O at 298.15 K. *J. Phys. Chem. A* **1998**, *102*,
735 2155–2171.

736 (44) Hargreaves, G.; Kwamena, N. O. A.; Zhang, Y. H.; Butler, J. R.; Rushworth, S.; Clegg, S.
737 L.; Reid, J. P. Measurements of the Equilibrium Size of Supersaturated Aqueous Sodium
738 Chloride Droplets at Low Relative Humidity Using Aerosol Optical Tweezers and an
739 Electrodynamic Balance. *J. Phys. Chem. A* **2010**, *114* (4), 1806–1815.

740 (45) Hale, G. M.; Querry, M. R. Optical Constants of Water in the 200-Nm to 200-Mm
741 Wavelength Region. *Appl. Opt.* **1973**, *12*, 555–563.

742 (46) Kedenburg, S.; Vieweg, M.; Gissibl, T.; Giessen, H. Linear Refractive Index and
743 Absorption Measurements of Nonlinear Optical Liquids in the Visible and near-Infrared
744 Spectral Region. *Opt. Mater. Express* **2012**, *2* (11), 1588–1611.

745 (47) Toon, O. B.; Pollack, J. B.; Khare, B. N. The Optical Constants of Several Atmospheric
746 Aerosol Species: Ammonium Sulfate, Aluminum Oxide, and Sodium Chloride. *J.*
747 *Geophys. Res.* **1976**, *81* (33), 5733–5748.

748 (48) Toon, O. B.; Pollack, J. B.; Khare, B. N. The Optical Constants of Several Atmospheric
749 Aerosol Species: Ammonium Sulfate, Aluminum Oxide, and Sodium Chloride. *J.*
750 *Geophys. Res.* **1976**, *81* (33), 5733–5748.

751 (49) Butler, T. J. A.; Miller, J. L.; Orr-Ewing, A. J. Cavity Ring-Down Spectroscopy
752 Measurements of Single Aerosol Particle Extinction. I. The Effect of Position of a Particle
753 within the Laser Beam on Extinction. *J. Chem. Phys.* **2007**, *126* (17), 174302:1-174302:7.

754 (50) Miller, J. L.; Orr-Ewing, A. J. Cavity Ring-down Spectroscopy Measurement of Single
755 Aerosol Particle Extinction. II. Extinction of Light by an Aerosol Particle in an Optical
756 Cavity Excited by a Cw Laser. *J. Chem. Phys.* **2007**, *126* (17), 174303.1-174303.7.

757 (51) Davies, J. F.; Miles, R. E. H.; Haddrell, A. E.; Reid, J. P. Temperature Dependence of the
758 Vapor Pressure and Evaporation Coefficient of Supercooled Water. *J. Geophys. Res.*
759 **2014**, *119* (18), 10.931-10.940.

760 (52) Miles, R. E. H.; Reid, J. P.; Riipinen, I. Comparison of Approaches for Measuring the
761 Mass Accommodation Coefficient for the Condensation of Water and Sensitivities to

762 Uncertainties in Thermophysical Properties. *J. Phys. Chem. A* **2012**, *116* (44), 10810–
763 10825.

764 (53) Langridge, J. M.; Richardson, M. S.; Lack, D. A.; Brock, C. A.; Murphy, D. M.
765 Limitations of the Photoacoustic Technique for Aerosol Absorption Measurement at High
766 Relative Humidity. *Aerosol Sci. Technol.* **2013**, *47* (11), 1163–1173.

767

768

769 TOC Graphic

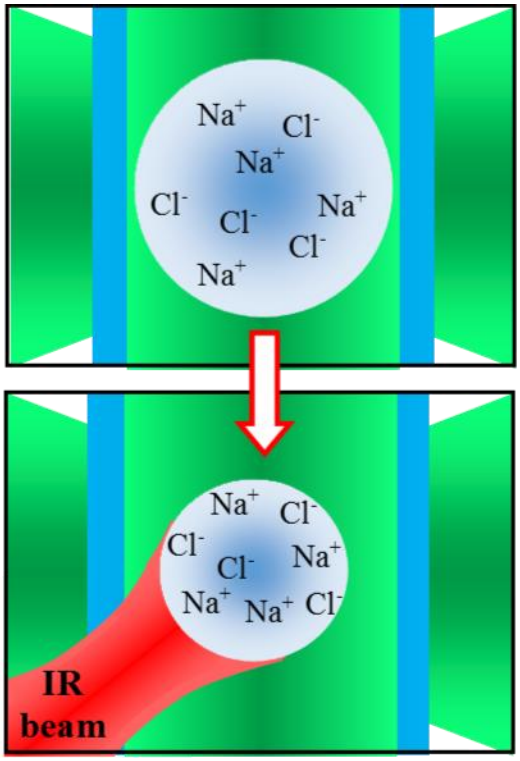

770